Attitude Estimation with Albedo Interference on Sun Sensor Measurements

Demet Cilden-Guler*
Istanbul Technical University, 34469 Istanbul, Turkey
Hanspeter Schaub†
University of Colorado Boulder, Boulder, Colorado 80303-0429
and
Chingiz Hajiyev‡ and Zerefsan Kaymaz§
Istanbul Technical University, 34469 Istanbul, Turkey

A three-axis attitude estimation scheme is presented using a set of albedo interfered coarse sun sensors (CSSs) of Earth, which are inexpensive, small in size, and light in power consumption. For modeling the interference, a two-stage albedo estimation algorithm based on autoregressive model is proposed. The algorithm does not require any data, such as albedo coefficients, spacecraft position, sky condition, or ground coverage, other than albedo measurements. The results are compared with five albedo models on the basis of two reference conditions. The estimated albedo is fed to the CSS measurements for correction. The corrected CSS measurements are processed under three estimation techniques with two different sensor configurations. The relative performance of the attitude estimation schemes when using different albedo models is examined.

Nomenclature

A	=	area, m^2
a_j	=	inverse variance of the sensor j
B	=	magnetic field, nT
$[BN]$	=	direction cosine matrix from inertial coordinates to body coordinates
$[BR]$	=	direction cosine matrix from reference coordinates to body coordinates
b	=	sensor observation vector in the body coordinates
$dA, \Delta A$	=	incremental area, m^2
F	=	solar flux, W/m^2
$f(\cdot)$	=	system function
H	=	measurement matrix
$h(\cdot)$	=	measurement function
I	=	output current, A
K	=	Kalman gain matrix
N_A	=	number of differential areas
$\hat{n}$	=	unit normal vector
p	=	number of previous measurements
r	=	measurement model vector in the reference coordinates
r_{sc}	=	spacecraft position vector from an incremental area, m
$\hat{r}_{sc}$	=	spacecraft direction vector from an incremental area
$\hat{s}$	=	sun heading vector
U	=	zero-mean Gaussian noise vector with covariance Q
V	=	output voltage, V
$\tilde{V}$	=	zero-mean Gaussian noise vector with covariance R
w	=	zero-mean Gaussian noise vector with covariance $\tilde{Q}$
x_0	=	initial state with mean μ_0 and covariance P_0
x_k, X_k	=	state vector at time t_k
$\hat{y}$	=	prediction vector
y, Z	=	measurement vector
z_k	=	albedo measurement at time t_k
α	=	albedo coefficient
ε	=	zero-mean Gaussian noise vector with covariance R
$\sigma_{B/R}$	=	modified Rodrigues parameters in body coordinates with respect to reference
φ_i	=	ith model parameter
ω	=	angular velocity, rad/s
Ξ	=	scaling term

Subscripts

A	=	central point of dA on a planet
d	=	caused by the sun
I	=	instrument
in	=	incoming
max	=	maximum
out	=	outgoing
P	=	planet
s	=	sunlit
sc	=	spacecraft
α	=	caused by albedo

I. Introduction

SPACECRAFT instruments need to be oriented to achieve mission directives in space. Depending on the mission, there may be strict performance requirements in terms of attitude estimation or necessity to a safe-mode operation or sanity checks. For these purposes, additional attitude sensors, such as magnetometers and sun sensors, can be used with less accuracy, but less power need, lower cost, and smaller size. Sun sensors are frequently used in both planet-orbiting satellites and interplanetary spacecraft missions in the solar system. They can be divided into two classes as fine or digital sun sensors (DSSs) and coarse sun sensors (CSSs), which are commonly used in a form of photodiodes [1]. Coarse sun sensors function almost proportional to the cosine angle between the boresight of the sensor and the sun direction vector from the spacecraft. They are often used on platforms, including multiple CSSs.

A spacecraft close enough to the sun and a planet receives electromagnetic radiation of direct solar flux; reflected radiation, namely,

*Ph.D. Candidate, Aeronautics and Astronautics Engineering Department, Visiting Scholar, Aerospace Engineering Sciences Department, University of Colorado Boulder; currently Teaching Assistant, Astronautics Engineering Department, Istanbul Medeniyet University. Student Member AIAA.
†Professor and Glenn L. Murphy Endowed Chair, Aerospace Engineering Sciences Department. Fellow AIAA.
‡Professor, Aeronautical Engineering Department.
§Professor, Meteorological Engineering Department.

albedo; and emitted radiation of that planet. The solar flux is the largest source of radiation for the spacecraft, whereas the albedo is the fraction of sunlight incident and reflected light from the planet. The spacecraft can be exposed to albedo when it sees the sunlit part of the planet (Fig. 1). The albedo values vary depending on the seasonal, geographical, and diurnal changes, as well as the cloud coverage. The most reflectance is caused by thickest, highest clouds, whereas the least by snowing clouds [2]. The CSS not only measures the light from the sun, but also the albedo of the planet [3]. So, the albedo interference of a planet can cause anomalous sun sensor readings. According to Ref. [4], albedo might worsen the sun pointing accuracy more than 20 deg. On the other hand, albedo might be an important factor in selecting the characteristics of optical-sensor systems, such as cameras or star trackers, and in spacecraft thermal and power design. For example, Ref. [5] underlines that the thermal control system on the spacecraft must consider the light reflectance and emittance of the planets as it causes a highly dynamic variation in thermal load. Another study on a spacecraft thermal analysis is carried out to evaluate the thermal conditions for temperature stability of sensitive instrument and radiators by using the albedo data from the Clouds and the Earth's Radiant Energy System (CERES) instruments [6] of NASA.

The mathematical model of the sun sensors can include diffusive and specular reflections from the planet, which represent the perturbed sun sensor measurements. In Ref. [7], perturbed sun sensor measurements are validated by the telemetry data of Ørsted satellite. The currents of the modeled CSSs are improved about three times more than the case not including any albedo model on the measurements in Ref. [7] and four times in Ref. [8]. A sun heading estimation algorithm is also applied by O'Keefe and Schaub [9] using extended Kalman filter (EKF). The sun direction is estimated with an accuracy under 4 deg based on albedo-interfered CSS and rate gyro (RG) measurements, and 10 deg without RGs despite the fact that an underdetermined sun sensor coverage is considered in the study [9].

References [10,11] present extended consider Kalman filter based on modified Rodrigues parameters (MRPs) for CSS calibration. The presented filters require inertial attitude measurements, but they give scale factor accuracy less than 1% and misalignment accuracy about 1 deg even under poor attitude knowledge. Another calibration filter is proposed for photodiodes through the estimation of attitude and calibration parameters simultaneously [12]. An arbitrary number of photodiodes along with an albedo model are calibrated using both an EKF and an unscented filter. The filter estimates improve the sun vector measurements by 10 deg and attitude by 1 deg by combining a three-axis magnetometer (TAM) and RG in the study. To make the albedo model lighter in computations, two constant albedo coefficients are applied rather than various spatial data in Ref. [13]. From the analyses, the errors are reduced by taking the average albedo coefficient as 0.105 instead of 0.30. Even though the presented model provides a significantly better CSS accuracy for most of the times than uncorrected outputs, its predictions based on 0.30 value may occasionally overcorrect the CSS. This overcorrection causes an

increase on the sensor error. It is stated that the detailed mathematical model, including the albedo coefficient changes depending on the active surface elements, can be used for the most accurate case, but it is computationally expensive for online usage. Reference [13] concludes that because of the albedo model complexity, it is more reasonable to use a filter on the sun sensor that restricts the sensor not sensitive to the albedo. This suggestion might be more suitable for DSSs. In Ref. [14], a less complex albedo model is generated via polynomial functions with 13 parameters for each albedo component, including functions based on latitude and longitude. The polynomial is fitted to the reflectivity data set from Earth Probe Total Ozone Mapping Spectrometer (TOMS) instead of using excessive data in lookup tables. The work also estimates the spacecraft attitude states with 1 deg accuracy in nominal mode and 2 deg in worst mode by EKF with 0.5% noisy measurements from TAM and corrected CSS.

The main purposes of our study were to estimate the albedo by using a simple model with less parameter dependency than any albedo models, and to estimate the attitude by comprising the corrected CSS measurements. The estimation process using only the CSS platform and using it along with TAM is presented to be considered during the sanity checks and/or in the safe-mode operations of a spacecraft missions or in the validation algorithm of other sensors' outputs. This aids the mission by making the albedo estimates available for the other subsystems.

As a simple model, autoregressive (AR) albedo model is proposed. Here, the purpose is to estimate the albedo without using any data related to albedo coefficients that depend on position, time, ground, and cloud coverage parameters. Autoregressive model or enhanced versions of the AR model are widely used in forecasting geomagnetic storm indices and estimating gyro drifts as well as wind speed [15–18], but to the best of our knowledge, it is used in albedo estimation for the first time in this study. The CSS measurement equations contain disturbances, most notably due to the albedo of Earth, which is dependent on too many parameters. Therefore, modeling albedo is complex and computationally heavy for online usage. In the meanwhile, AR is a simple model based on only a couple of parameters in accordance with how many measurements are used. However, attitude information of a spacecraft is necessary to estimate the albedo based on the AR model. So, an attitude estimation procedure is also presented using the estimated albedo. Reference [7] indicates that it is possible to perform a three-axis attitude estimation by using only CSSs with albedo interference, but the nondifferentiability of the output equations makes the estimation harder. This is why the attitude estimation procedure proposed in this study is composed by estimating the albedo first and correcting the CSS after. In this way, any albedo model is not considered in the last output equations in the attitude estimation filter.

The remainder of this paper is organized as follows. Section II presents the albedo and CSS mathematical models. The attitude estimation filter and AR-model-based two-stage albedo estimation filter used in this study are given in Secs. III and IV, respectively. In Sec. V, the analysis and results of several scenarios for the albedo data of Earth, albedo effects on CSSs, possible albedo models, and attitude estimation filters are presented and discussed. The last section summarizes and concludes the paper.

II. Albedo and CSS Modeling

A. Mathematical Model for the Albedo of a Planet

The mathematical model for the total albedo from a planet affecting an instrument (e.g., CSS) on a spacecraft is given in this section. The parameters affecting the albedo model can be itemized as the attitude and position of the spacecraft, field of view (FOV) of an instrument, placement of other instruments (that might block/shadow), and albedo coefficients related to several parameters (such as ground coverage, seasonal changes, and cloudiness).

The generic vectors can be described as unit normal vector $\hat{\boldsymbol{n}}$, sun heading vector $\hat{\boldsymbol{s}}$, and direction vector from A to $B\,\hat{\boldsymbol{r}}_{AB}$. In Fig. 2, $\hat{\boldsymbol{n}}_A$ and $\hat{\boldsymbol{n}}_I$ are the unit normal vectors of the differential area dA on the planet and the instrument cell, respectively; $\hat{\boldsymbol{s}}_P$ and $\hat{\boldsymbol{s}}_I$ are the sun heading vectors of the planet and of the instrument cell, respectively. Here, the position vector of the instrument from the incremental area is $\boldsymbol{r}_{AI}$ and
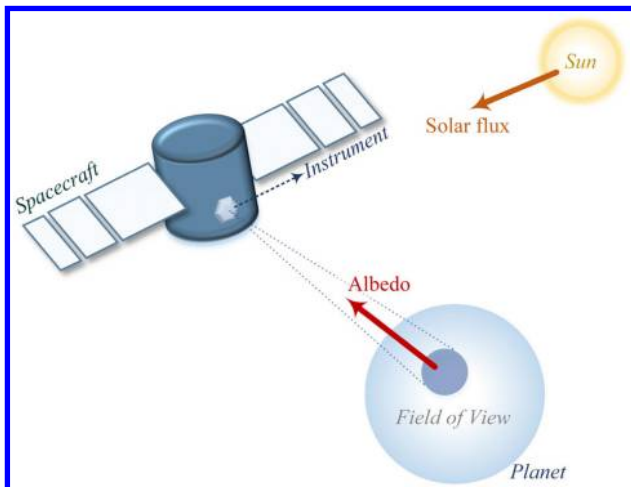

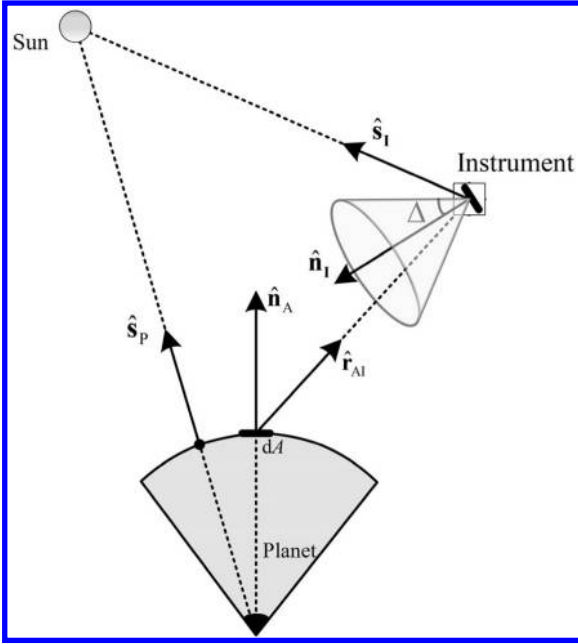**Fig. 1   Illustration of considered radiation sources on a spacecraft.**

Fig. 2 Illustration of the unit normal, sun, and spacecraft heading vectors.

the unit direction vector is $\hat{r}_{AI} = r_{AI}/\|r_{AI}\|$. The direction vector of the spacecraft from dA can be expressed as $\hat{r}_{sc}$.

The differential areas 1) on the sunlit portion of the planet where $(\hat{s}_P \cdot \hat{n}_A > 0)$ forming A_s (sunlit region), 2) in the FOV of the instrument with a half-angle of Δ where $(-\hat{r}_{AI} \cdot \hat{n}_I \geq \cos(\Delta))$ forming A_I (instrument FOV region), 3) in the maximum FOV of the instrument cell where $(\hat{r}_{AI} \cdot \hat{n}_A > 0)$ forming $A_{I_{\max}}$ (maximum area that can be seen from the instrument cell), and 4) in the FOV of the spacecraft where $(\hat{r}_{sc} \cdot \hat{n}_A > 0)$ forming A_{sc} (spacecraft FOV region) can be used for the total albedo calculations contributing to the instrument or the spacecraft. The total area that is sunlit and visible to the instrument results in $A \equiv A_s \cap A_I$ (see Fig. 3).

The solar flux reaching to a point is found as $F_{\text{sun}}(\hat{s} \cdot \hat{n})$ (in W/m^2) when using the generic vectors. So, the solar flux reaching the incremental area (F_{in}) is [3]

$$F_{\text{in}} = F_{\text{sun}}(\hat{s}_P \cdot \hat{n}_A) \qquad (1)$$

where F_{sun} is the solar constant at the top of the atmosphere (TOA). The mean value of the solar flux at the mean distance of the sun–planet is called solar constant, which slightly changes depending on the solar cycle and the distance of the planet from the sun. The solar constant value for Earth is 1366.1 W/m^2. The incoming solar flux is both absorbed and reflected partially. The reflected portion is proportional to the albedo coefficient α as

$$\begin{aligned} F_{\text{out}} &= \alpha F_{\text{in}} \\ &= \alpha F_{\text{sun}}(\hat{s}_P \cdot \hat{n}_A) \end{aligned} \qquad (2)$$

Using the conservation of energy [3], the irradiance due to the albedo of the planet at the position of the spacecraft is

$$F_\alpha = \frac{F_{\text{sun}}}{\pi} \iint_A \frac{\alpha(\hat{s}_P \cdot \hat{n}_A)(\hat{r}_{AI} \cdot \hat{n}_A)(-\hat{r}_{AI} \cdot \hat{n}_I)}{\|r_{AI}\|^2} dA \qquad (3)$$

where F_{sun} is the solar constant at the TOA; $\hat{s}_P$ is the sun heading vector of the planet, $\hat{n}_A$ and $\hat{n}_I$ are the unit normal vectors of dA and the instrument cell, respectively; and $\hat{r}_{AI}$ is the unit direction vector to the instrument from dA. Equation (3) is rewritten in a summation form to obtain a discrete version as [19]

$$F_\alpha = \frac{F_{\text{sun}}}{\pi} \sum_{i=1}^{N_A} \frac{\alpha(\hat{s}_P \cdot \hat{n}_{A_i})(\hat{r}_{AI_i} \cdot \hat{n}_{A_i})(-\hat{r}_{AI_i} \cdot \hat{n}_I)}{\|r_{AI_i}\|^2} \Delta A \qquad (4)$$

where N_A is the number of differential areas (ΔA) inside the intersectional area A.

B. Albedo Coefficients

Albedo coefficient α is the ratio of the reflected and incoming solar radiation over a unit area that ranges from 0 to 1. As it is described in the previous section, the data are required to comprise albedo based on the latitude and longitude of a planet, and it might optionally include information of date/time, cloudiness, etc. The most reflective planet in the solar system is Venus by its global Bond albedo around 0.76 [20]. The average albedo of Earth evolved over time, but converged to 0.29 in the mean in the last 40 years and had only 0.2% interannual variability on global mean albedo [21]. In order not to model a complex albedo close to the real case, which depends on many parameters as discussed, a constant global albedo coefficient can be used. However, the use of this kind of straightforward planet interference might be insufficiently accurate [13].

To determine the total albedo affecting the instrument, the planet should be divided into grids based on the albedo data size. Figure 4 shows an illustration of the albedo contributions from each grid element within the FOV to the instrument. The albedo data might include irregularities on the latitude and longitude (see Fig. 5). The grid elements to be considered can be determined using their central points. The grid element with the central point within the FOV can be considered as an active element. In Fig. 5, regular and irregular grid examples are given. Even the area seen is the same (red elliptical area); the active grid elements to be used (blue rectangular areas) for the calculations differentiate. Another method to apply here is to use an interpolation technique [22], such as inverse distance weighting, kriging, bi-cubic, nearest neighbor, etc., so as to use the exact area of interest in the calculations. It is also possible to convert the irregular grids into the regular version.

The albedo data of Mars can be obtained from the instrument Thermal Emission Spectrometer (http://tes.asu.edu/) on the Mars Global Surveyor spacecraft launched in 1996. The data have irregularities in the sense of latitude and longitude intervals.

The albedo data of Earth can be obtained from instruments, such as TOMS (https://ozoneaq.gsfc.nasa.gov/) and CERES (https://ceres.larc.nasa.gov/). The TOMS measures the albedo of the atmosphere of Earth in the near-ultraviolet region. The data are mapped with a grid size of 180×288 and a latitude and longitude resolution of $1 \times 1.25°$.
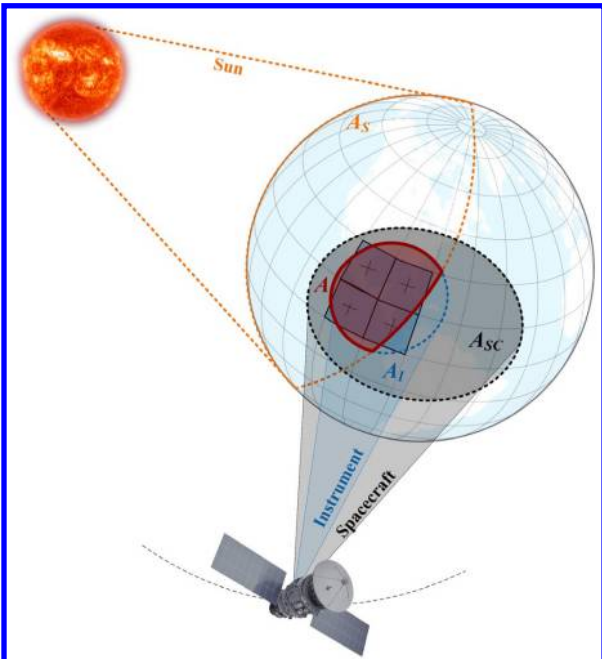

Fig. 3 Illustration of the observed illuminated area.
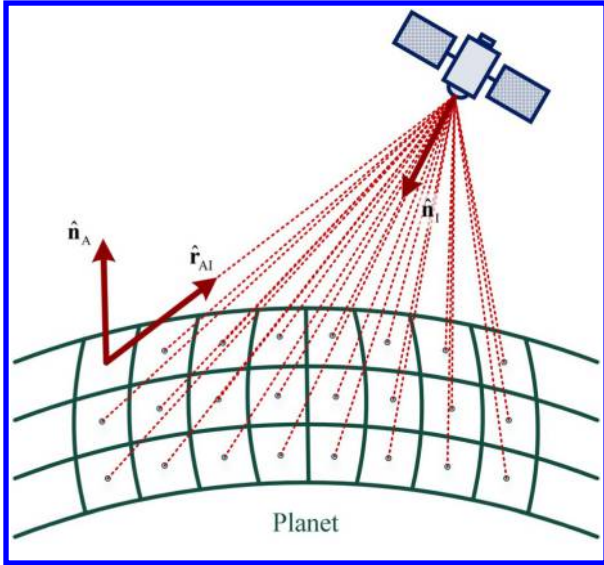
Fig. 4 Illustration of the albedo influence on an instrument from observed incremental areas of a planet.

The most recent data are obtained from the Earth Probe mission between 1996 and 2006. The CERES albedo data up to with $1 \times 1°$ resolution can be found with surface or TOA options under clear-sky and all-sky conditions. The clear-sky monthly mean TOA fluxes from CERES are provided completely cloud free according to Moderate Resolution Imaging Spectroradiometer data with 1 km resolution [23,24]. There are several satellites having CERES instrument onboard, such as Tropical Rainfall Measuring Mission, Terra, Aqua, Suomi National Polar-orbiting Partnership, and NOAA-20. Terra and Aqua satellites have two CERES instrument pairs to provide an enhanced product quality. The hourly, daily, and monthly satellite pair (Terra–Aqua) data are available starting from 2002. A sample albedo coefficient data of Earth from CERES averaged over 2018 is presented in Fig. 6.

C. Modeling of CSS Measurements in the Presence of Albedo

As the CSS senses any light received, the light reflected from a celestial body will also affect the sensor. Here, one celestial body is considered close enough to a spacecraft for modeling the CSS measurements without having any blockage to the FOV of the sensor from the structural components of the spacecraft. Adding more than one celestial body to the simulations is possible by adding another albedo
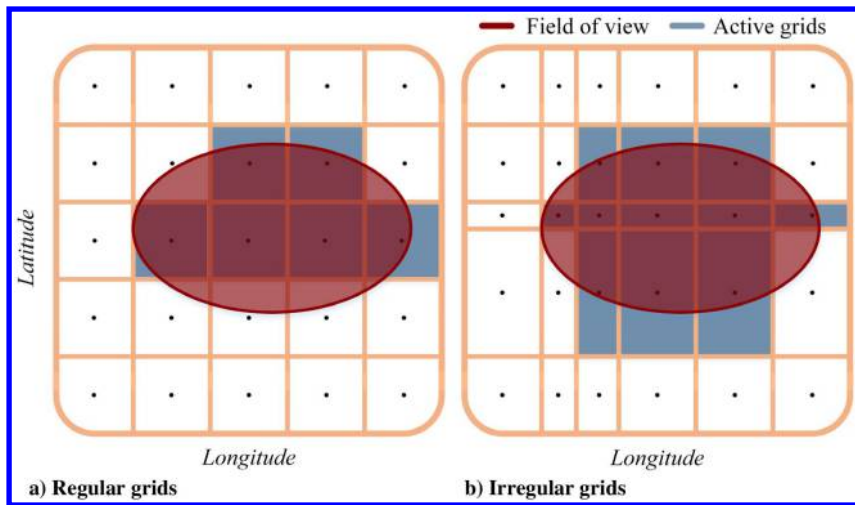

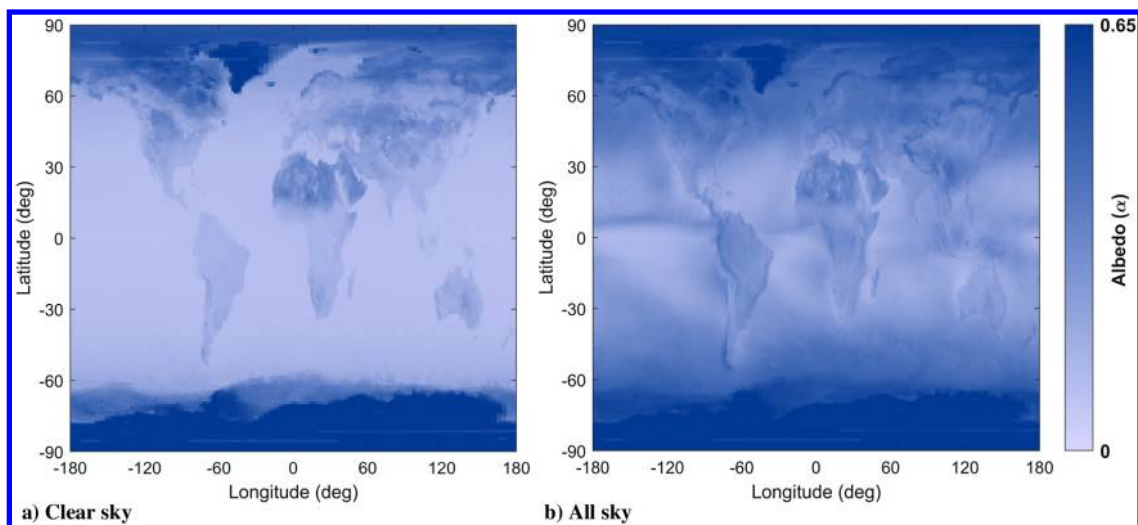**Fig. 5 Illuminated FOV area with a) regular and b) irregular grid examples.**

Fig. 6 Albedo coefficients averaged over CERES 2018 monthly data under a) clear-sky and b) all-sky conditions.
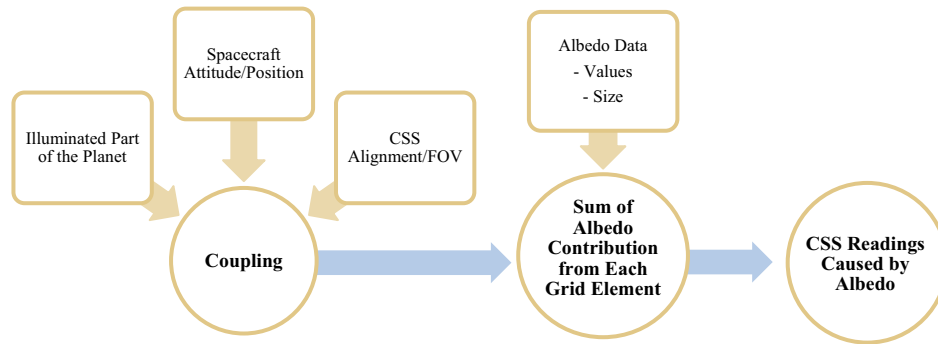
Fig. 7   Process for simulating the CSS albedo readings.

summing term. The structural blockage can be avoided at the design stage or modeled in the FOV of the CSS. The process of simulating the CSS readings excited by the albedo of a planet is given in Fig. 7.

The output current of the CSS is proportional to the angle between the boresight of the sensor and the direction of the light source in general [3]. By using the solar irradiance formula on an instrument as $F_{\text{sun}}(\hat{s}_I \cdot \hat{n}_I)$, the output current generated from the CSS can be expressed as

$$I_d = \begin{cases} I_{\max} \dfrac{F_{\text{sun}}}{F_{\text{cal}}}(\hat{s}_I \cdot \hat{n}_I) & \text{if } (\hat{s}_P \cdot \hat{n}_A > 0) \cap (\hat{s}_I \cdot \hat{n}_I \geq \cos(\Delta)) \\ 0 & \text{otherwise} \end{cases} \quad (5)$$

where F_{cal} is the calibration flux determined during ground testing, and $I_{\max}$ is the possible maximum output current of the CSS. The current of the CSS contributed from albedo is written as [7]

$$I_\alpha = \begin{cases} I_{\max} \dfrac{F_{\text{sun}}}{F_{\text{cal}}} \displaystyle\sum_{i=1}^{N_A} \dfrac{\alpha(\hat{s}_P \cdot \hat{n}_{A_i})(\hat{r}_{AI_i} \cdot \hat{n}_{A_i})(-\hat{r}_{AI_i} \cdot \hat{n}_I)}{\pi \|r_{AI_i}\|^2} \Delta A, & \text{if } \Delta A \in A \\ 0 & \text{if } \Delta A \notin A \end{cases} \quad (6)$$

The resulting CSS current gives

$$I = I_d + I_\alpha + \varepsilon_{\text{CSS}} \quad (7)$$

where ε_{CSS} is zero-mean Gaussian noise on the measurements. One might need to use voltage outputs depending on the given instrumental data sheet. The voltage output can be calculated in a similar manner by including the maximum voltage of CSS, $V_{\max}$, instead of $I_{\max}$, in calculating V_d and V_α. The resulting voltage of the CSS is

$$V = V_d + V_\alpha + \varepsilon_{\text{CSS}} \quad (8)$$

The presented CSS readings in a current or a voltage format belong to only one photodiode, and the calculations need to be repeated for as many photodiodes as are available.

III.   Gaussian Estimation Filters

The general estimation state-space problem is expressed as

$$x_k = f(x_{k-1}) + w_k \quad (9)$$

$$y_k = h_k(x_k) + \varepsilon_k \quad (10)$$

where $f(\cdot)$ is the system and $h(\cdot)$ is the measurement function, x_k is the state vector at a time t_k, w_k is the zero-mean Gaussian noise vector with the covariance of Q, y_k is the measurement vector, and ε_k is the zero-mean Gaussian noise vector with the covariance of R_k. The initial state is x_0 with mean μ_0 and covariance P_0; its probability density function can be denoted as $p(x_0) = N(x_0|\mu_0, P_0)$. Approximations based on Kalman filtering can be represented using the Gaussian filter

(GF) technique [25]. This technique uses the parameters μ_k, P_k in $p(x_k|y_{1:k}) = N(x_k|\mu_k, P_k)$ for the distribution of state estimation by two stages. The first stage is composed of predictions using the system function to determine the predicted mean:

$$\mu_k^- = \int f(x_{k-1})N(x_{k-1}|\mu_{k-1}, P_{k-1}) \, dx_{k-1} \quad (11)$$

and the predicted covariance

$$P_k^- = \int (f(x_{k-1}) - \mu_{k-1})(f(x_{k-1}) - \mu_{k-1})^T \\ \times N(x_{k-1}|\mu_{k-1}, P_{k-1}) \, dx_{k-1} + Q \quad (12)$$

The second stage updates the predictions using the measurements as

$$\hat{y}_k = \int h_k(x_k)N(x_k|\mu_k^-, P_k^-) \, dx_k \quad (13)$$

$$\Psi_k = \int (x_k - \mu_k^-)(h_k(x_k) - \hat{y}_k)^T N(x_k|\mu_k^-, P_k^-) \, dx_k \quad (14)$$

$$\Phi_k = \int (h_k(x_k) - \hat{y}_k)(h_k(x_k) - \hat{y}_k)^T N(x_k|\mu_k^-, P_k^-) \, dx_k \quad (15)$$

The innovation can be found as

$$e_k = y_k - \hat{y}_k \quad (16)$$

with the innovation covariance

$$S_k = \Phi_k + R_k \quad (17)$$

which is used in constituting the Kalman gain as

$$K_k = \Psi_k S_k^{-1} \quad (18)$$

Finally, the posterior mean and the associated covariance can be found as

$$\mu_k = \mu_k^- + K_k e_k \quad (19)$$

$$P_k = P_k^- - K_k S_k K_k^T \quad (20)$$

The integrals given in Eqs. (11–15) can be approximated using different Kalman-type filters [26,27]. The attitude of a spacecraft can be estimated using conventional approaches, namely, the EKF [28] or unscented Kalman filter, which is derivative free [29], based on nonlinear system and measurement functions defined in Eqs. (9) and (10). An EKF is used in this study, and the attitude is represented using MRPs indicated with $\sigma_{B/R}$ symbol, which is in body coordinates with respect to the reference (inertial) coordinates [30,31].

Another approach is using deterministic attitude determination techniques called single-frame methods (SFMs) as a substep to make the attitude part of the measurements linear with respect to the states [32–36]. The SFM-based preprocessing step is also implemented before the update stage of the filter by minimizing Wahba's loss function [37]:

$$L(A_k) = \frac{1}{2}\sum_j a_{j_k}|b_{j_k} - [BR]_k r_{j_k}|^2 \qquad (21)$$

where $[BR]$ is the direction cosine matrix (DCM) from reference coordinates to body coordinates, a_j is the inverse variance of the sensor j, b_j is the sensor observation vector in the body coordinates, and r_j is the measurement model vector in the reference coordinates. The attitude can be determined by SFM and used in the GFs as linear attitude measurements. The loss function can be minimized using one of the SFM methods, namely, singular-value decomposition (SVD), Quaternion Estimator, q, Fast Optimal Attitude Matrix (FOAM), etc. [33,38].

The attitude measurement from the SFM is

$$\tilde{y}_k = Hx_k + \varepsilon_k \qquad (22)$$

where the part of the measurement matrix corresponding to the attitude states is an identity matrix; $\tilde{y}_k$ is the attitude measurement with covariance $\tilde{R}_k$, which is updated inherently by SFM. The innovation in Eq. (16) is replaced by

$$e_k = \tilde{y}_k - \hat{y}_k \qquad (23)$$

and Eq. (17) by

$$S_k = HP_k^- H^T + \tilde{R}_k \qquad (24)$$

Single-frame-method-aided Kalman filters are expected to benefit from having the initial attitude determined by SFM, especially for the transient region of the estimations. According to Ref. [33], the SVD method is faster than the q method and more robust than the computationally fast methods (e.g., FOAM and Estimator of the Optimal Quaternion [39]). In this regard, SVD, SVD-aided EKF, and conventional EKF estimation methods are implemented to the computer simulations in this work.

In this study, a spacecraft is considered to have two or three measurement sensors out of CSS, TAM, and RG, because these sensors are commonly used for spacecraft missions.

Each CSS can be modeled using Eq. (7), which gives the current generated by one CSS in the body frame. For the platform, the sun direction measurement vector can be obtained as

$$y_{css} = \sum_{i=1}^{N_{css}} I_i \cdot \hat{n}_{css_i} \qquad (25)$$

where $\hat{n}_{css_i}$ is the unit normal vector of the ith CSS cell, and N_{css} is the number of CSSs.

Three-axis magnetometer measurements can simply be modeled as

$$B_{tam} = [BN]B_{model} + \varepsilon_{tam} \qquad (26)$$

where $[BN]$ is the DCM from inertial to the body frame, ε_{tam} is the zero-mean Gaussian magnetometer measurement noise vector, and B_{model} is the magnetic field model output, such as those of the International Geomagnetic Reference Field (IGRF), World Magnetic Model, dipole model, etc. [40,41]. International Geomagnetic Reference Field is used for this work.

Rate gyros are used to model the angular velocity of the spacecraft. The measurements can be modeled as

$$\omega_{RG} = \omega_{BN} + \varepsilon_{RG} \qquad (27)$$

where ω_{RG} are the body measured angular rates based on the spacecraft dynamics model angular velocity ω_{BN} of the body frame with respect to the inertial frame, and ε_{RG} is the zero-mean Gaussian gyroscope measurement noise vector.

IV. Two-Stage Albedo Estimation Filter Using AR Model

This section presents a two-stage estimation using AR time-series approximation for the planet's albedo estimation. The AR model is based on simple summing term, which uses a number of previous measurements, and a noise term as

$$z_k = \sum_{i=1}^{p}(\varphi_i z_{k-i}) + \varepsilon_k \qquad (28)$$

where z_k represents one component of the albedo measurements (the difference between the sun sensor measurements in the body frame and the sun direction model transformed into body frame using the spacecraft's attitude information), φ is the model parameter, p is the number of previous measurements to be used, and ε_k is the zero-mean Gaussian noise. Akaike criterion can be used to determine the order of the AR model [42]. The first stage estimates the AR model parameters using the recursive least-squares method. By substituting the collected measurements of z_k, the matrix form of the measurement equation can be expressed as

$$Y_k = \tilde{Z}_k \underset{\sim}{\Phi}_k + \varepsilon_k \qquad (29)$$

where $Y_k = z_k$, $\tilde{Z}_k = [z_{k-1} \ z_{k-2} \ \cdots \ z_1]$, and $\underset{\sim}{\Phi}_k = [\varphi_1 \ \varphi_2 \ \cdots \ \varphi_{k-1}]^T$. The formula for the estimation of the model parameters can be written as [17]

$$\underset{\sim}{\Phi}_{k+1} = \underset{\sim}{\Phi}_k + \Xi_k(Y_k - \tilde{Z}_k \underset{\sim}{\Phi}_k) \qquad (30)$$

Here, the scaling (Ξ_k) in the correction term is determined by

$$\Xi_k = \frac{1}{1 + \tilde{Z}_k \Gamma_k \tilde{Z}_k^T} \Gamma_k \tilde{Z}_k^T \qquad (31)$$

where

$$\Gamma_k = (\tilde{Z}_k^T \tilde{Z}_k)^{-1} \qquad (32)$$

The model parameters estimated from Eq. (30) can be used in the second stage. The linear system is defined as [17]

$$X_k = F_k X_{k-1} + B_k U_k \qquad (33)$$

and the measurement is

$$Z_k = HX_k + V_k \qquad (34)$$

where $X_k = [z_k \ z_{k-1} \ \cdots \ z_{k-p+1}]_{1\times p}^T$ is the state vector, $U_k = [\varepsilon_k \ 0 \ \cdots \ 0]_{1\times p}^T$ is the zero-mean Gaussian noise vector with the process noise covariance matrix $\underset{\sim}{Q}$, V_k is the zero-mean Gaussian noise vector with the measurement covariance matrix $\underset{\sim}{R}$, $H = [1 \ 0 \ \cdots \ 0]_{1\times p}$ is the measurement matrix, and F_k and B are given as

$$F_k = \begin{bmatrix} \varphi_1 & \varphi_2 & \cdots & \varphi_p \\ 1 & 0 & \cdots & 0 \\ \vdots & \vdots & \ddots & \vdots \\ 0 & 0 & 0 & 0 \end{bmatrix}_{p\times p} \qquad (35)$$

$$B = \begin{bmatrix} 1 & 0 & \cdots & 0 \\ 0 & 0 & \cdots & 0 \\ \vdots & \vdots & \ddots & \vdots \\ 0 & 0 & \cdots & 0 \end{bmatrix}_{p \times p} \tag{36}$$

The Kalman-type filtering algorithm based on the defined system and the measurement functions is able to estimate the albedo state vector using Eqs. (16–20). The innovation in Eq. (16) is replaced by

$$e_k = Z_k - H\mu_k^- \tag{37}$$

The innovation covariance in Eq. (17) is replaced by

$$S_k = HP_k^{-1}H^T + \underset{\sim}{R} \tag{38}$$

Finally, the Kalman gain in Eq. (18) is replaced by

$$K_k = P_k^- H^T S_k^{-1} \tag{39}$$

for representing the Kalman filtering of the second-stage estimation. By using the two-stage estimation form, the albedo of a planet can be estimated at each time step.

V. Analysis and Results

A. Albedo Data of Earth and Sun Sensor Measurements

Eleven years of Synoptic TOA and surface fluxes and clouds (SYN) 4.1 edition of Terra–Aqua satellite pair CERES data product is used with $1 \times 1°$ global grid of Earth. The global albedo for 11 years from 2008 to 2018 is presented using box plots for each month in Fig. 8 under clear-sky and all-sky conditions. The small range of the box plots of each month demonstrates that the interannual albedo does not significantly change over the years for any month. While the averages slightly change or do not differ in years, values depending on the month grossly vary under both sky conditions with a similar trend. The trend of the plots is similar for the clear-sky and all-sky cases. The lines in the figures are Fourier series model-based fitted curves to the mean values from the box plots of each month identified as the red color for the all-sky condition and blue for the clear-sky condition. The all-sky condition is almost as twice as the clear-sky albedo averages. From the data, the global average of the albedo over the years and months is found to be about 0.23 under clear-sky condition and 0.37 under all-sky condition.

The albedo coefficients given in Fig. 9 are 11 years (2008–2018) averaged over four consecutive seasons as season 1 (December to February), season 2 (March to May), season 3 (June to August), and season 4 (September to November). The values are distributed based
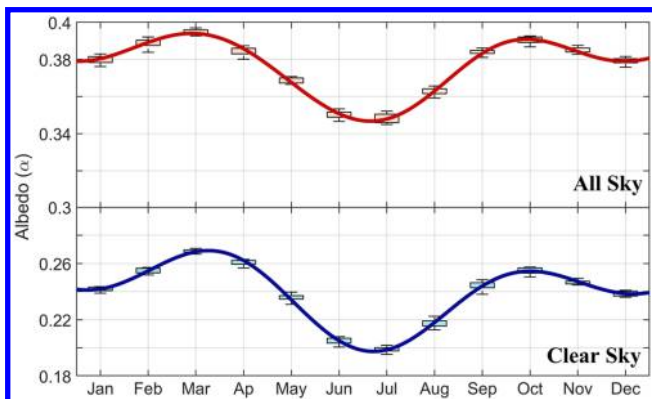
Fig. 8 Monthly albedo box plots for 11 years under clear-sky (bottom) and all-sky (top) conditions.

on the data under clear-sky and all-sky conditions globally. The albedo differentiates globally with the seasonal changes and with the sky conditions. The coefficients for each season and sky condition are presented by the maps prepared using the Hammer–Aitoff projection [43]. The null grids are shown with the white color, which is not excessive for the monthly mean data, and the continents with the black lines. In this way, the albedo dependency on the land coverage can be realized, which is more noticeable in the clear-sky condition than the all-sky condition. The all-sky case mostly has a cloudy sky that causes the neighboring regions having similar albedo values and reduces the ground cover effects. In addition to the cloud formations, the highest reflectivity is observed in the polar regions and Greenland [14].

The albedo coefficients in Tables 1 and 2 are also 11 year averaged values using spatial and seasonal scales. The spatial scales include global, tropics, polar, and mid-latitude regions at the northern (N) and southern (S) hemispheres, whereas the seasonal scales have four time intervals as described. The values are averaged based on clear-sky (Table 1) and all-sky (Table 2) conditions. The cells with no data are ignored in the averaging process. Several remarks can be itemized by looking at the albedo variations as

1) The maximum averaged albedo is at the polar regions under all cases.

2) Albedo is the most effective in boreal winter (December to February) at the northern hemisphere and in austral winter (June to August) in the southern hemisphere under all cases.

3) The peak values are found in the same spatial regions under the all-sky condition (minimum at the tropics and maximum at the polar south region).

4) The peak values are found in slightly different spatial regions under clear-sky conditions.

5) All values are greater in the all-sky case compared to the clear-sky case.

6) The lookup table can be implemented for attitude estimation purposes by dividing the planet into spatial regions and seasonal periods for less computation instead of using every grid on the planet over several years.

For analyzing the effects of the albedo of Earth on CSS measurements, it is possible to use an arbitrary year rather than the exact year of spacecraft flight because the average values do not differ significantly in years by referring to Fig. 8. The data sample averaged over arbitrarily chosen year, 2018, is employed (Fig. 6). A scenario is performed for observing the albedo effects on the CSS measurements particularly.

Here, CSS platforms are put on every face for convenience in the observation of the albedo of Earth. Photodiode placement on each CSS platform is illustrated in Fig. 10 in platform coordinates $\{\hat{p}_1, \hat{p}_2, \hat{p}_3\}$. Each CSS has $\Delta = 60$ deg half-FOV angle and is assumed to read a maximum of 1 A under direct sunlight.

For the first spacecraft setup, a fixed craft with no rotational dynamics is placed on the Sun–Earth line at 800 km altitude for simplicity in observing the CSS outputs. In Fig. 11, the positions of the sun, spacecraft, and Earth are illustrated without scaling. In this scenario, a symmetrical behavior might be expected in CSS platform outputs on spacecraft–face–counterparts in terms of only sun exposure except for $+x$ and $-x$ directions. Here, $+x$ is pointing to the sun and $-x$ to Earth. However, albedo also excites the CSS. The satellite faces are numbered, respectively, for $+x, +y, +z, -x, -y$, and $-z$ directions in Fig. 11. For the analysis, face 4 ($-x$ direction) of the satellite, which is exposed only to the albedo of Earth and not to the sun, is used. To inspect the parameter dependence of albedo, two parameters—altitude and longitude—are tested by differentiating one parameter and fixing the other. The FOV of each CSS on face 4, in which the outer frame is marked with a black line, can be seen in Fig. 12. The base albedo map behind each region is shown in Fig. 6a.

For better illustrative analysis, CSS 1 on face 4 is presented. The CSS FOV region in the sunlit area of the planet in Fig. 13 is marked with the colored base albedo map. The observed area is getting larger with rising altitude. However, even if the observed area is getting larger, the current readings of each CSS caused by the albedo—without any noise on the sensor—decrease and converge to zero
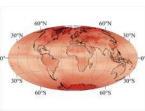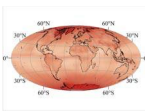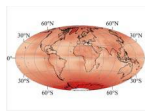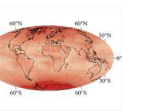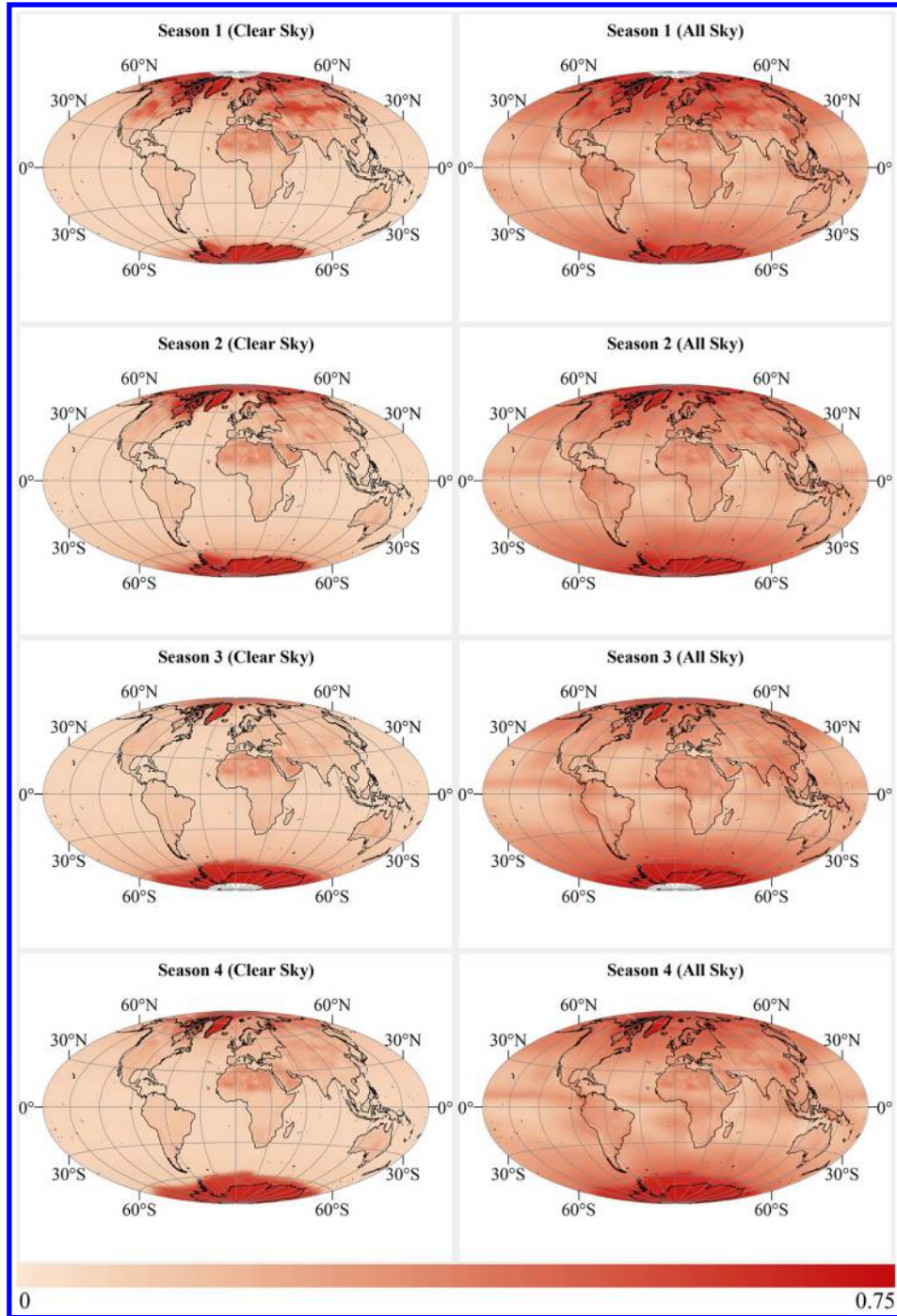
Fig. 9 Eleven-year averaged global albedo coefficients over four seasons under clear-sky (left) and all-sky (right) conditions.

Table 1   Eleven-year averaged albedo coefficients over regions and seasons indicated (clear sky)

Averaging scale	Season 1 (Dec. to Feb.)	Season 2 (March to May)	Season 3 (June to Aug.)	Season 4 (Sept. to Nov.)
Global	0.3017	0.2999	0.2704	0.2852
Polar North ($60° - 90°$N)	0.5310	0.5068	0.3093	0.4224
Mid-latitude North ($30° - 60°$N)	0.2602	0.1798	0.1370	0.1792
Tropics ($30°$N $- 30°$S)	0.1210	0.1178	0.1195	0.1177
Mid-latitude South ($30° - 60°$S)	0.1017	0.1476	0.1779	0.1165
Polar South ($60° - 90°$S)	0.4947	0.5475	0.6082	0.5905

Table 2   Eleven-year averaged albedo coefficients over regions and seasons indicated (all sky)

Averaging scale	Season 1 (Dec. to Feb.)	Season 2 (March to May)	Season 3 (June to Aug.)	Season 4 (Sept. to Nov.)
Global	0.4346	0.4270	0.4110	0.4252
Polar North (60° − 90°N)	0.5910	0.5692	0.4636	0.5461
Mid-latitude North (30° − 60°N)	0.4309	0.3465	0.3016	0.3536
Tropics (30°N − 30°S)	0.2350	0.2242	0.2361	0.2315
Mid-latitude South (30° − 60°S)	0.3205	0.3687	0.3986	0.3414
Polar South (60° − 90°S)	0.5955	0.6261	0.6550	0.6535

when going up from 500 to 20,000 km altitude (see Fig. 14) because of the inverse square law of the light intensity.

It is known that there is a large dependency on latitude, but it is sometimes assumed that there is only a small dependency on longitude [4,14,44]. To inspect this assumption, the longitude dependency of the albedo on a CSS is examined for both cases (clear sky and all sky). The CSS readings depending on the longitude changes are seen in Fig. 15 for {60°N, 30°N, 0°, 30°S, 60°S} latitudinal lines. Even if it was expected to have similar current readings caused by albedo when differentiating the longitude at high latitudes, outputs on panels 1 and 5 of the figures still highly depend on the longitude change of the spacecraft. In fact, 0° latitude differs the least in the clear-sky case. The standard deviations are calculated, respectively, as $\sigma_{\text{clear}} = [0.018 \ 0.006 \ 0.004 \ 0.012 \ 0.018]$ for the clear-sky condition and $\sigma_{\text{all}} = [0.017 \ 0.005 \ 0.014 \ 0.011 \ 0.018]$ for the all-sky condition. However, there is no regular trend seen for differentiating longitudes on the same latitude line; therefore, their effects need to be taken into account. The results from this examination are special to our case, but point out that the albedo value at the instrument depends on the longitude. There might be some cases where the albedo is

having almost a constant value on a latitude line or a region if several conditions meet simultaneously, which is a rare case.

B. Spacecraft Attitude Estimation Using the Albedo-Interfered Sun Sensors

In the second setup, the simulations are performed for a spacecraft with the principal moment of inertia $I = \text{diag}[0.055 \ 0.055 \ 0.017]\,\text{kg} \cdot \text{m}^2$ on an almost circular near-Earth orbit with 730 km average altitude and with inclination $i = 96.5$ deg starting on 1 March 2018 or 1 June 2018 at 2400 hrs Coordinated Universal Time. The spacecraft is tumbling during the simulations on an orbit propagated by employing the Simplified General Perturbation Version 4 (SGP4) model introduced by Ref. [45]. (The SGP4 source code is available at http://celestrak.com/publications/AIAA/2006-6753/.) The sun direction is formulated using the model presented by Vallado [46]. The CSSs are processed at 1 Hz and corrupted by Gaussian zero-mean noise with a standard deviation of 2% (unitless).

The first part of this section is devoted to analyzing the albedo estimation using different albedo models. For this purpose, the models are divided into roughly two different categories as albedo-data-based models (empirical albedo models) and the AR albedo model. The estimation procedures for each model category can be seen in Figs. 16a and 16b, respectively. The attitude information for the sun direction vector transformation from inertial to body frame is assumed to be estimated by using star trackers with 1 arc second accuracy without considering any misalignments on the sensors. In Fig. 16a, the albedo estimation procedure is based on the model requiring to find the sunlit area within the FOV of the sensor and to obtain the albedo coefficient data. Albedo estimation based on the AR model, on the other hand, does not require any of this information but a two-stage estimation. The AR albedo model is also tested for a one-stage estimation filter, but the results were not promising so that only the two-stage estimation filter based on the AR model is proposed to be used for albedo estimation. The estimation procedures use the albedo measurements
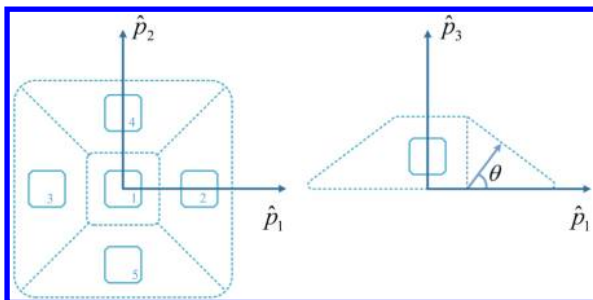
Fig. 10   Illustration of CSS placement on each platform.
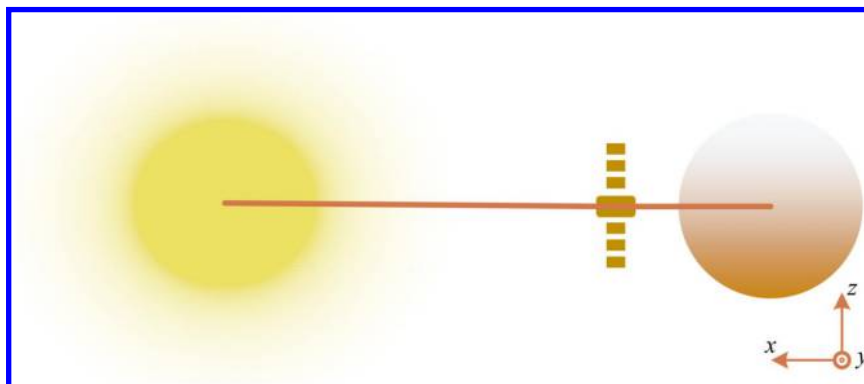
Fig. 11   Illustration of the sun, spacecraft, and Earth positions for scenario 1.
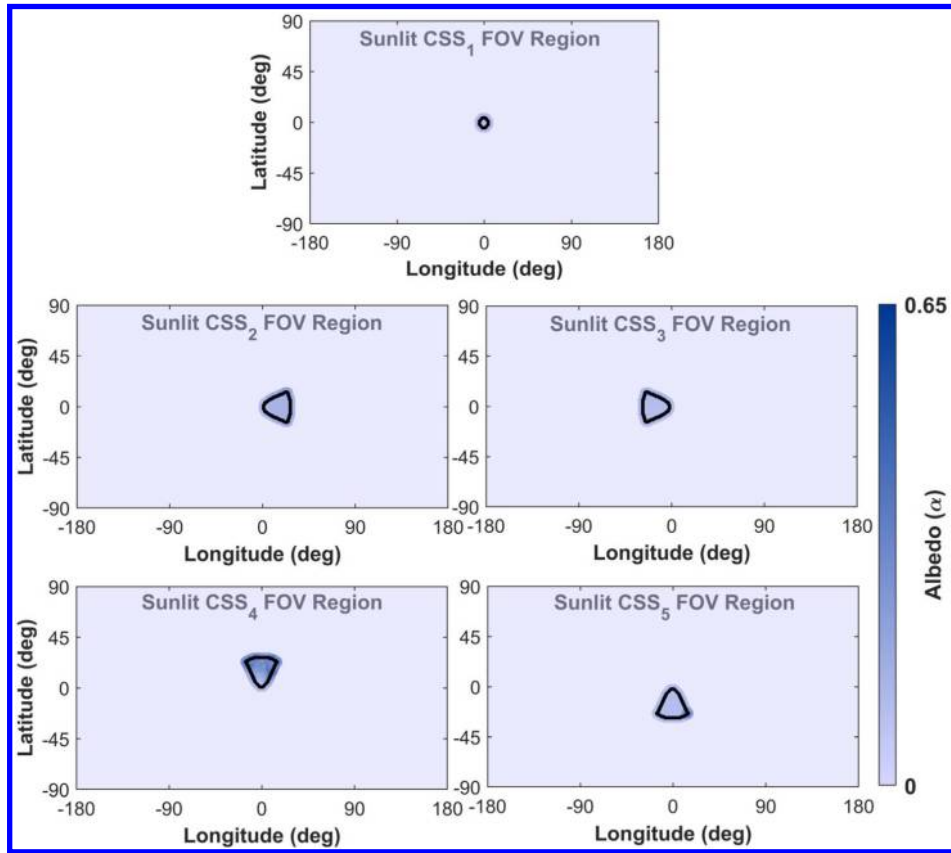
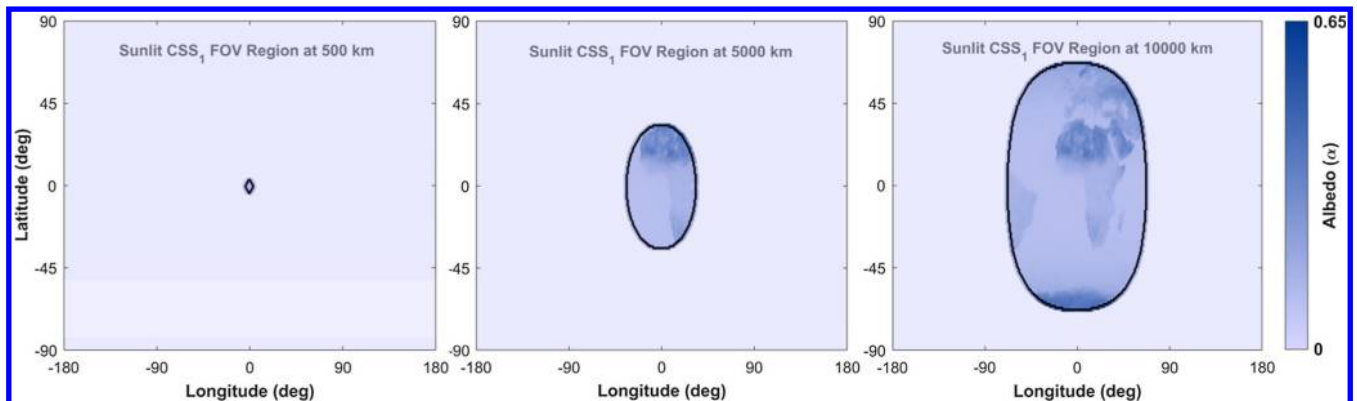Fig. 12   CSS FOV on face 4 of the satellite at 800 km altitude.

Fig. 13   CSS 1 FOV on face 4 of the satellite at three different altitudes (left to right: 500, 5000, and 10,000 km).

generated by the difference between the sun direction measurement vector of the CSS and the modeled sun direction vector transformed into the body frame. However, as the albedo measurements are dependent on the CSS measurements directly, possible sensor-related continuous or time-varying biases will be treated as part of the albedo as well.

The considered albedo models are presented in Table 3. The first two rows list the reference models used in creating the CSS measurements and the rest are selected to see the differences of the model outputs with respect to the references. More than 11 years of CERES albedo coefficient data of Earth are available for the public. So, the first reference model is based on 1 month averaged data over March 2018 for the clear-sky condition, whereas the second reference averaged over 11 years of data from 2008 to 2018 for July under the clearsky condition. The first five albedo models are named by sequential numbers and produced using CERES data or a constant value, and the last row shows the AR albedo model. Model 1 uses the albedo data

averaged over March 2018 under the all-sky condition. Model 2 uses the albedo data averaged over the whole year of 2018 under the clearsky condition. Model 3 uses the lookup table presented in Table 1. Models 4 and 5 are based upon the given constant values. Model 3 differs according to which spatial region of the instrument is looking at and in which season the spacecraft is flying. The references are based on two different months in our case, so model 3 uses two seasons from the lookup table as seasons 2 and 3 corresponding to reference models 1 and 2, respectively.

The albedo model outputs of reference models 1 and 2 are given for three orbits in Fig. 17. There is no albedo contribution during eclipse, as seen from the figure. Therefore, a portion of the simulation is analyzed. The first 1000 s is selected to be analyzed as the differences between two reference models are more distinct. The albedo model outputs from several albedo models are presented in Fig. 18 for comparing each one of them with reference model 1 on the left panel and reference model 2 on the right. As the same condition
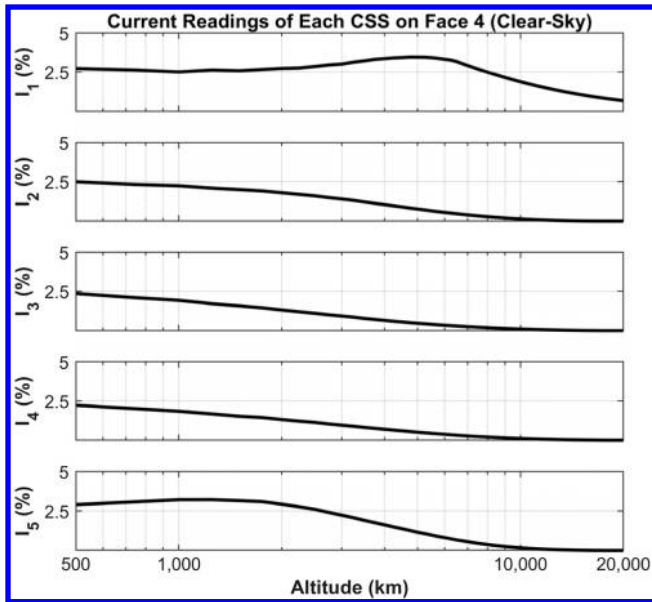
Fig. 14 Altitude-dependent CSS current outputs on face 4 of the satellite.

and configuration for the spacecraft and instrument are used, models 1–5 do not differentiate from one case to another, except model 3 with different seasonal values. From the results, it can be said that only the AR albedo model follows the reference models for both cases. Among the other albedo models, model 4, which uses a constant albedo value $\alpha = 0.29$ over all spatial points on Earth, is superior under reference model 1 case and model 2 under reference model 2 case.

A complementary table is composed of albedo rms error and the computational time for each model in Table 4. The rms errors are calculated based on the albedo model outputs and the estimations with respect to the reference models. The rms errors confirm the results of Fig. 18. Albedo data-driven models are also processed under a conventional estimation filter to make a fair comparison with the AR albedo model, which is based on a two-stage estimation. The albedo estimations based on models 1–5 give more than three times better accuracy than the AR model-based estimations. However, models 1–5 depend on many parameters, unlike the AR model. In the meantime, the computational burden is lighter when it comes to the AR model, as seen from Table 4. The AR model does not require any data processing at the beginning, and the total processing and estimation speed is around six times faster than the others.

The limitation of the AR albedo model might be caused by inadequate or faulty albedo measurements, as it highly depends on the measurements. For example, if there is a sensor-related bias on CSS in addition to the albedo, this will be compensated by the AR albedo model estimation procedure; yet, the albedo estimation will not represent the actual albedo this time. This might cause an issue for the other subsystems in need of estimated albedo information, such as solar panels. On-ground calibration is suggested for preventing such a problem.

Attitude information is assumed to be known with high accuracy in the first part. As the AR albedo model is greatly dependent on the albedo measurements with a necessity of attitude information, albedo estimations are most likely to be disrupted in the case of no proper attitude information like a malfunction of the star trackers. If there are no star tracker outputs available, then magnetometers and/or sun sensors could conceivably be used for attitude determination purposes. It is possible to use them separately as a single sensor in recursive estimation methods or together for an improved estimation. In the analysis, the estimations are first presented using TAM and CSS pair, and then CSS without TAM. Using TAM measurements in the estimations is performed by closing the switches for TAM and magnetic field model boxes seen in Figs. 19a and 19b, and open switches are for not using them.

The albedo is assumed to be in the form of reference model 2 based on the 11 year averaged July CERES albedo data under the clear-sky condition in all cases. A wrong albedo model in the form of model 4 and AR model that does not require any information other than CSS measurements and attitude of the spacecraft is considered in the attitude and albedo estimation algorithms for comparison. The RG-driven kinematic motion model is used for the attitude estimation filters in this study, but the use of a dynamic model with no RGs is also an option [47,48].

The "Albedo-data-based model" box in Fig. 19a represents the wrong albedo model (model 4) in the analysis. The CSS outputs are corrected by using the albedo models before using it in the attitude estimation methods. Attitude is represented by MRPs ($\sigma_{B/R}$), where B stands for the body and R for the reference (Earth-centered inertial) coordinates in the simulations, but transformed into Euler 3–2–1 angles in degrees for presentation. The estimation error levels of the components vary between different simulations possibly due to the randomized values used in the models and the filters. Therefore, the attitude error norms are presented instead of giving the results in component by component. The attitude error norms of the listed estimation methods are given in Fig. 20a using model 4. The same procedure is applied by replacing model 4 with the AR model, as presented in Fig. 19b. But this time, the attitude error is a little more, especially in the transient region until compensation at around 600th s seen in Fig. 20b.
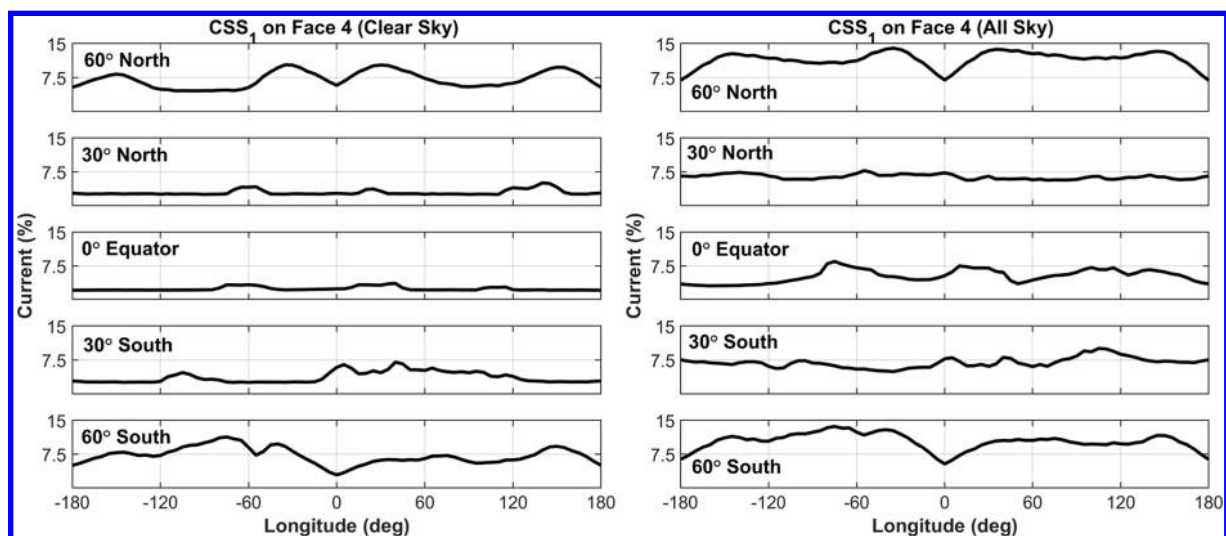

Fig. 15 Longitude-dependent CSS 1 current outputs on face 4 of the satellite at 800 km under clear-sky (left) and all-sky (right) conditions.
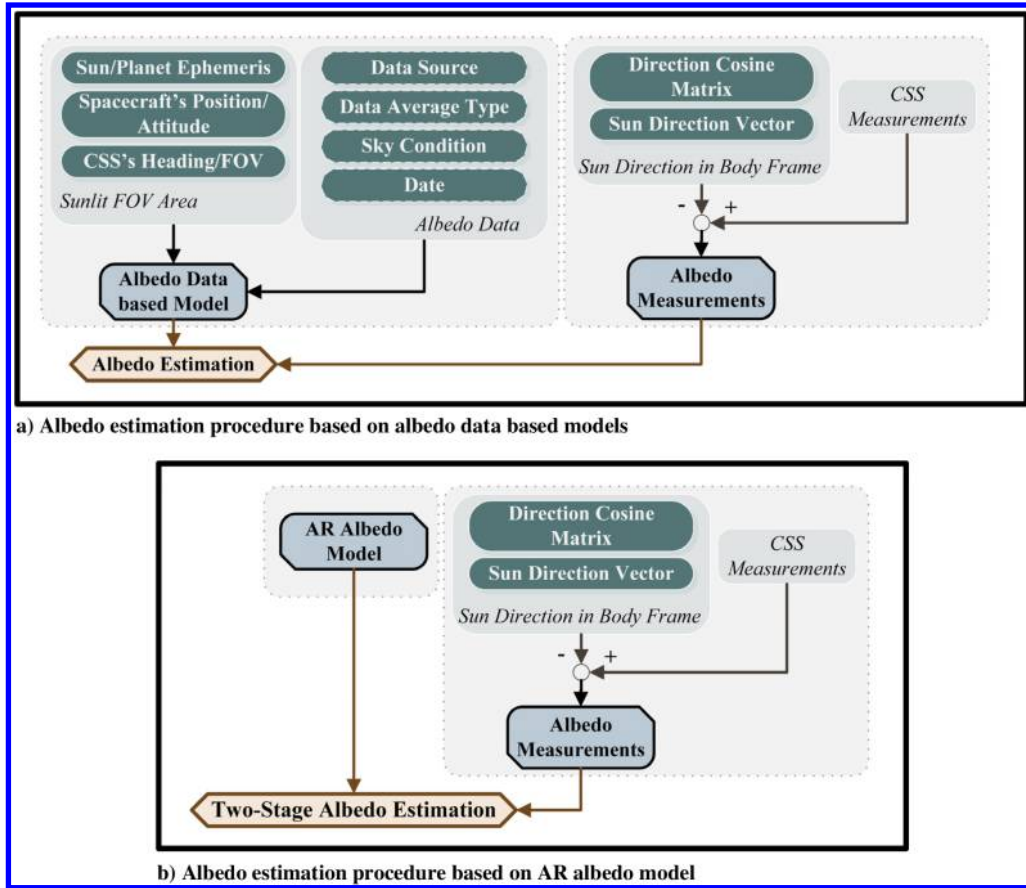
Fig. 16 Albedo estimation procedure based on a) albedo-data-based models and b) AR albedo model.

Table 3 Details of the models used for albedo estimation

Model name	Albedo data	Average type	Sky condition	Additional information
Reference model 1 Ref. [1]	CERES	Monthly average March 2018	Clear sky	——
Reference model 2 Ref. [2]	CERES	Monthly average July 2008–2018	Clear sky	——
1	CERES	Monthly average March 2018	All sky	——
2	CERES	Yearly average 2018	Clear sky	——
3	CERES	Yearly average 2008–2018	Clear sky	Lookup table based on spatial and seasonal regions (see Table 1)
4	Constant	——	——	$\alpha = 0.29$
5	Constant	——	——	$\alpha = 0.15$
AR	——	——	——	No need to find the sunlit FOV area; model parameters to be estimated first

It is possible to estimate the spacecraft attitude using only one vector observation in the recursive estimation methods; CSS measurements are used in this case. The structures of model 4 and the AR model-based estimation filters are shown in Figs. 19a and 19b, respectively,

with open switches for magnetic-field-related blocks. Having only CSS with albedo interference makes the results deteriorate more, as seen in Figs. 21a and 21b. The mean attitude estimation errors are given in Table 5.
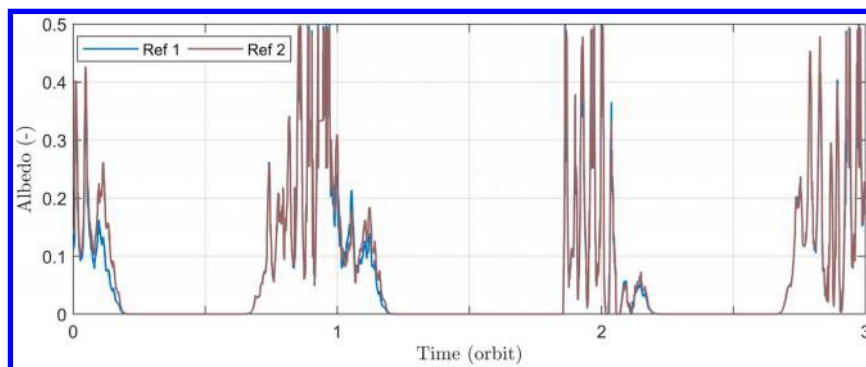

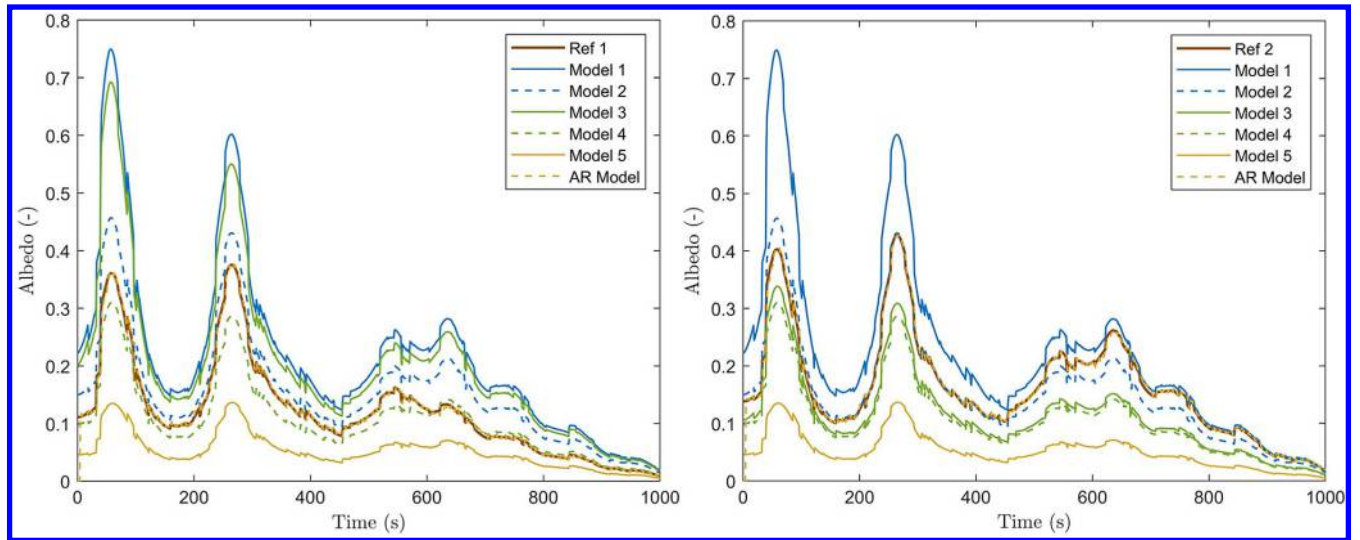Fig. 17 Albedo model outputs of reference models 1 and 2 for three orbits.

Fig. 18 Albedo model outputs of several models compared to reference model 1 (left) and reference model 2 (right).

Table 4 Performance comparison of the albedo models considered

| Model name | RMS error | | | | Computational time, s | |
| | Model only | | Estimation | | | |
	Ref. [1]	Ref. [2]	Ref. [1]	Ref. [2]	Data processing	Model processing and estimation
1	0.1201	0.0902	0.0028	0.0027	1.3082	0.0188
2	0.0395	0.0216	0.0028	0.0027	1.4038	0.0188
3	0.0991	0.0612	0.0028	0.0027	0.0014	0.0188
4	0.0277	0.0647	0.0028	0.0027	0.0004	0.0188
5	0.0897	0.1274	0.0028	0.0027	0.0004	0.0188
AR	——	——	0.0094	0.0111	——	0.0030

Table 6 is composed using normalized rms (nrms) errors of attitude estimation averaged over 100 Monte Carlo simulations, which confirms the results except that EKF gives slightly improved results than presented in Fig. 20b.

From the analyses, it is identified that albedo-data-based models (models 1–5) differ from the reference models case to case, but on the other hand, the AR albedo model follows the reference. So, it cannot be directly stated which model is the best among the five data-driven albedo models, and they can only be evaluated case by case. For a fair comparison in the estimation sense, a conventional estimation filter is applied to the albedo models that also follow the reference trend like the AR albedo model. This comparison is made under the assumption of having highly accurate attitude information from star trackers. In terms of computations, the AR albedo model processing and estimation speed is around six times faster than the others. Among the albedo-data-based models, model 4 ($\alpha = 0.29$) is found to be the best of confirming the first reference and model 2 (2018 yearly average) of confirming the second reference. Unfortunately, Model 3 underperformed expectations for our case. Based on these, it is recommended to use the AR albedo model because of its consistency between cases. However, the AR albedo model is limited with the used albedo measurements, which might include CSS-related bias. On-ground calibration is suggested for preventing such a problem.

Two sensor configurations and two albedo models (model 4 and AR model) are considered in the attitude estimation sense. Overall, EKF is an accurate attitude estimation method with less computational burden than the preprocessed filter (SVD-aided EKF) for TAM–CSS pair. It can be used in CSS-only case as well. The other attitude estimation methods can also be implemented using the proposed framework in Fig. 19. The TAM–CSS pair case provides the most accurate attitude estimation when using model 4 corrections. The CSS-only case, on the other hand, provides the most accurate attitude estimation when

using the AR model corrections. Therefore, the albedo model to be used can be determined based on the configuration as well.

VI. Conclusions

This study considers a spacecraft setup close enough to the sun and Earth receiving electromagnetic radiation of direct solar flux and reflected radiation, namely, albedo, in which both are sensed by the sun sensors. The albedo data of Earth are obtained from the CERES instrument. By evaluating the data, the maximum albedo of Earth is found in the polar regions and under all-sky conditions. Continental areas have higher albedo values, especially under clear-sky conditions. Albedo contributes to sun sensors from each incremental area of Earth in the sunlit area within the sensor FOV. The albedo intensity has a higher impact on sun sensors when getting closer to Earth.

The main purpose of this study was to find a simple model with less parameter dependency than the empirical albedo models. The second purpose was to estimate the attitude by comprising the corrected CSS measurements free from albedo so as to obtain better accuracy. The AR albedo model is proposed, which does not use albedo coefficients depending on the position, time, ground, and cloud coverage parameters. To the best of the authors' knowledge, the AR model is used in albedo estimation for the first time in this study. For comparison, five different models are evaluated under the albedo-data-driven model in addition to the AR albedo model. The two-stage albedo estimation filter is applied based on the AR model so as to mitigate the albedo error source from the CSS measurements and to feed into the necessary subsystems. It is proposed to use the AR albedo model because of its simplicity and consistency between cases. However, spacecraft attitude information is necessary to estimate the albedo based on the AR model. So, an attitude estimation procedure is also presented using the estimated albedo. The procedure is composed by estimating the albedo first and correcting the CSS after. In this way, it has the

a) Attitude estimation scheme based on albedo data based models

b) Attitude estimation scheme based on AR albedo model
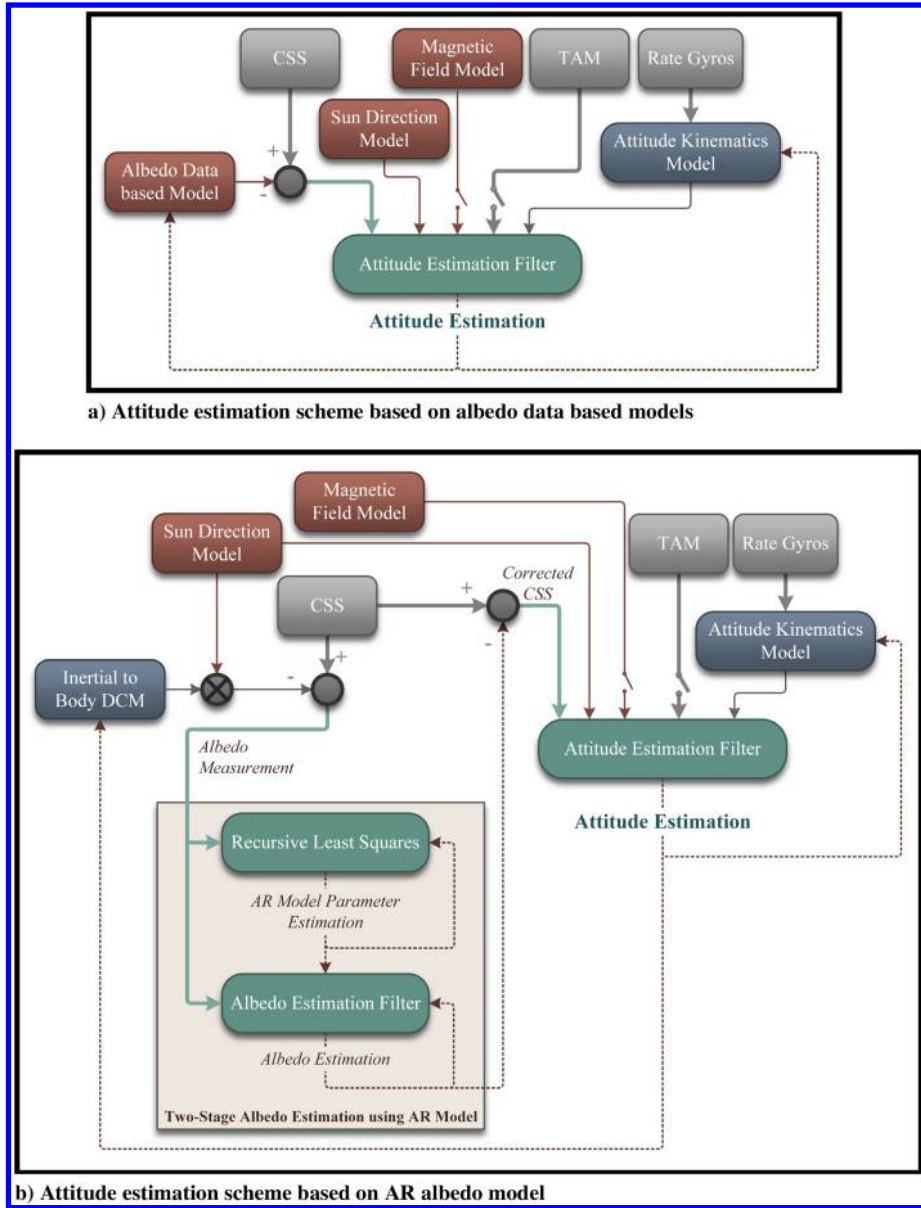
Fig. 19   Attitude estimation framework based on a) albedo-data-based models and b) AR albedo model.
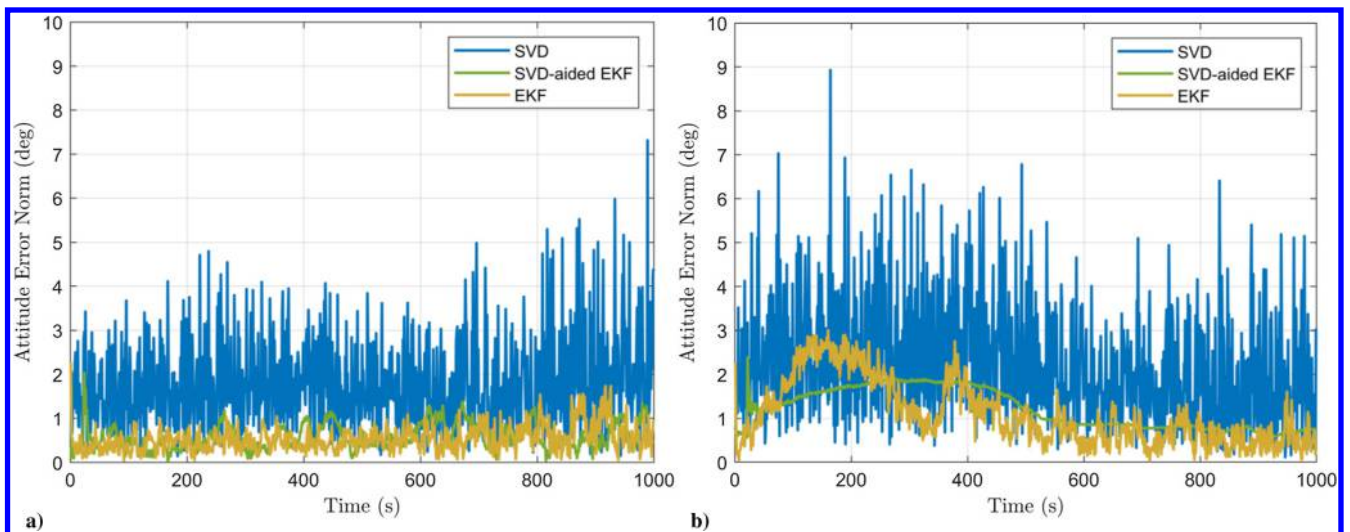

Fig. 20   Attitude error norms using TAM and CSS with albedo interference based on a) model 4 and b) AR model.
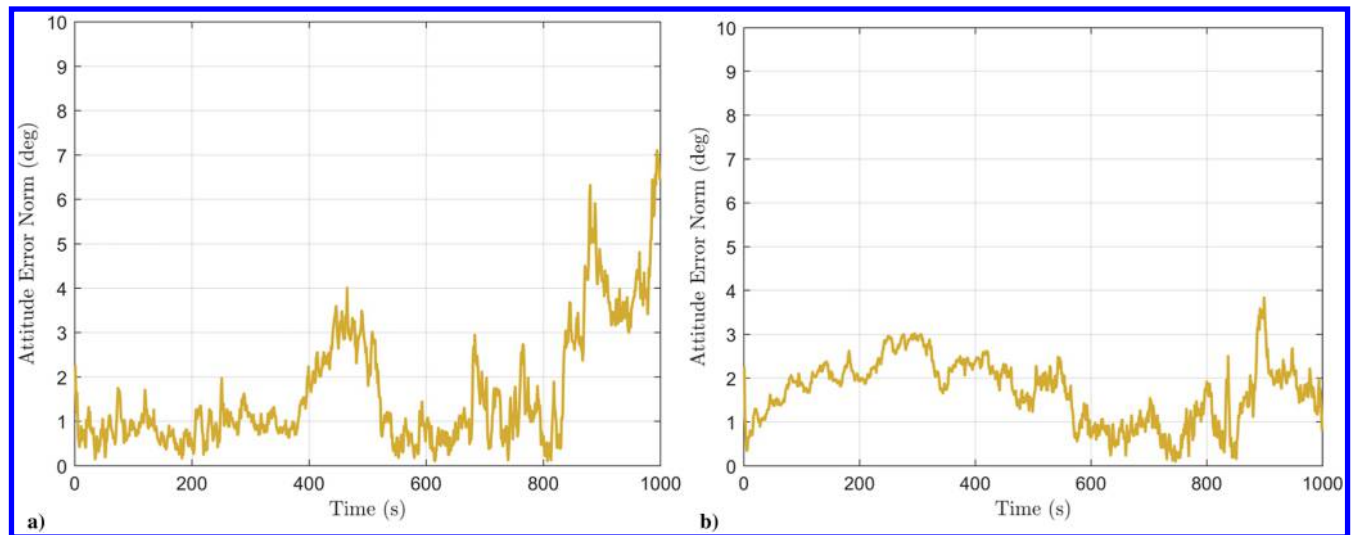
Fig. 21   Attitude error norms of EKF using CSS with albedo interference based on a) model 4 and b) AR model.

Table 5   Attitude angle estimation performance

		Mean attitude error, deg		
Sensor	Albedo model	SVD	SVD-aided EKF	EKF
TAM and CSS	4	1.87	0.58	0.54
	AR	2.35	1.45	1.09
CSS	4	— —	— —	2.45
	AR	— —	— —	1.92

Table 6   Performance comparison of the attitude estimation algorithms considered (averaged over 100 simulations)

		Attitude nrms error, %	
Sensor	Method	Model 4	AR model
TAM and CSS	SVD	1.20	1.82
	SVD-aided EKF	0.53	1.01
	EKF	0.38	0.38
CSS	EKF	2.34	1.70

advantage that any albedo model is not considered in the last output equations of the attitude estimation filter. The attitude is estimated in accordance with two different sensor configurations by the Kalman-type estimation filters. Three-axis attitude is estimated with around 4 deg accuracy using only CSS measurements without any correction and around 2 deg accuracy when CSS is corrected by the AR model.

Acknowledgments

References

[1] Markley, F. L., and Crassidis, J. L., "Sensors and Actuators," *Fundamentals of Spacecraft Attitude Determination and Control*, Springer, New York, 2014, pp. 123–181.
https://doi.org/10.1007/978-1-4939-0802-8_4

[2] Anon., "Earth Albedo and Emitted Radiation," NASA Goddard Space Flight Center TR NASA-SP-8067, Greenbelt, MD, 1971.

[3] Flatley, T. W., and Moore, W. A., "An Earth Albedo Model: A Mathematical Model for the Radiant Energy Input to an Orbiting Spacecraft Due to the Diffuse Reflectance of Solar Radiation from the Earth Below," NASA TM 104596, 1994.

[4] Bhanderi, D., and Bak, T., "Modeling Earth Albedo for Satellites in Earth Orbit," *AIAA Guidance, Navigation, and Control Conference and Exhibit*, AIAA Paper 2005-6465, Aug. 2005.
https://doi.org/10.2514/6.2005-6465

[5] Kuvyrkin, G. N., and Menshawy, T. M., "Earth's Albedo Input to a Low-Earth-Orbit Satellite Based on Local Albedo Coefficients," *Journal of Spacecraft and Rockets*, Vol. 53, No. 4, July 2016, pp. 792–796.
https://doi.org/10.2514/1.A33349

[6] Peyrou-Lauga, R., "Using Real Earth Albedo and Earth IR Flux for Spacecraft Thermal Analysis," *47th International Conference on Environmental Systems*, ICES Steering Committee Paper ICES-2017-142, 2017.

[7] Bhanderi, D., "Modeling Earth Albedo Currents on Sun Sensors for Improved Vector Observation," *AIAA Guidance, Navigation, and Control Conference and Exhibit*, AIAA Paper 2006-6592, Aug. 2006.
https://doi.org/10.2514/6.2006-6592

[8] Lopes, R. V. F., Silva, A. R., Relloso, J., Absi, G., and Jun, Y., "Analysis of Albedo Effects on Coarse Sun Direction Determination Algorithms," *22nd International Symposium on Space Flight Dynamics*, INPE (Brazilian Institute for Space Research), 2011.

[9] O'Keefe, S. A., and Schaub, H., "Sun-Direction Estimation Using a Partially Underdetermined Set of Coarse Sun Sensors," *Journal of the Astronautical Sciences*, Vol. 61, No. 1, 2014, pp. 85–106.
https://doi.org/10.1007/s40295-015-0058-9

[10] O'Keefe, S. A., and Schaub, H., "Consider-Filter-Based On-Orbit Coarse Sun Sensor Calibration Sensitivity," *Journal of Guidance, Control, and Dynamics*, Vol. 40, No. 5, May 2017, pp. 1300–1303.
https://doi.org/10.2514/1.G001692

[11] O'Keefe, S. A., and Schaub, H., "On-Orbit Coarse Sun Sensor Calibration Sensitivity to Sensor and Model Error," *AAS/AIAA Spaceflight Mechanics Meeting*, American Astronautical Soc. Paper 15-392, Jan. 2015.

[12] Springmann, J. C., and Cutler, J. W., "On-Orbit Calibration of Photodiodes for Attitude Determination," *Journal of Guidance, Control, and Dynamics*, Vol. 37, No. 6, Nov. 2014, pp. 1808–1823.
https://doi.org/10.2514/1.G000175

[13] Brasoveanu, D., and Sedlak, J., "Analysis of Earth Albedo Effect on Sun Sensor Measurements Based on Theoretical Model and Mission Experience," *AAS/GSFC 13th International Symposium on Space Flight Dynamics*, NASA, Washington, D.C., Vol. 1, 1998, pp. 435–447.

[14] Appel, P., "Attitude Estimation from Magnetometer and Earth-Albedo-Corrected Coarse Sun Sensor Measurements," *Acta Astronautica*, Vol. 56, Nos. 1–2, 2005, pp. 115–126.
https://doi.org/10.1016/j.actaastro.2004.09.001

[15] Ailliot, P., and Monbet, V., "Markov-Switching Autoregressive Models for Wind Time Series," *Environmental Modelling & Software*, Vol. 30, April 2012, pp. 92–101.
https://doi.org/10.1016/j.envsoft.2011.10.011

[16] Chandorkar, M., Camporeale, E., and Wing, S., "Probabilistic Forecasting of the Disturbance Storm Time Index: An Autoregressive Gaussian Process Approach," *Space Weather*, Vol. 15, No. 8, Aug. 2017, pp. 1004–1019.
https://doi.org/10.1002/2017SW001627

[17] Wang, D., Xu, X., Yao, Y., Zhu, Y., and Tong, J., "A Hybrid Approach Based on Improved AR Model and MAA for INS/DVL Integrated Navigation Systems," *IEEE Access*, Vol. 7, June 2019, pp. 82794–82808.
https://doi.org/10.1109/ACCESS.2019.2924593

[18] Narasimhappa, M., "Modeling of Inertial Rate Sensor Errors Using Autoregressive and Moving Average (ARMA) Models," *Gyroscopes —Principles and Applications* [Working Title], IntechOpen, U.K., 2019.
https://doi.org/10.5772/intechopen.86735

[19] O'Keefe, S. A., "Autonomous Sun-Direction Estimation Using Partially Underdetermined Coarse Sun Sensor Configurations," *Aerospace Engineering Sciences Graduate Theses & Dissertations*, Univ. of Colorado Boulder, Boulder, CO, 2015.

[20] Titov, D. V., Bullock, M. A., Crisp, D., Renno, N. O., Taylor, F. W., and Zasova, L. V., *Exploring Venus as a Terrestrial Planet*, Geophysical Monograph Series, Vol. 176, American Geophysical Union, Washington, D.C., 2007, pp. 121–138.
https://doi.org/10.1029/176GM08

[21] Stephens, G. L., O'Brien, D., Webster, P. J., Pilewski, P., Kato, S., and Li, J., "The Albedo of Earth," *Reviews of Geophysics*, Vol. 53, No. 1, 2015, pp. 141–163.
https://doi.org/10.1002/2014RG000449

[22] Smith, M. J., Goodchild, M. F., and Longley, P. A., "Surface and Field Analysis," *Geospatial Analysis: A Comprehensive Guide to Principle Techniques and Software Tools*, 6th ed., The Winchelsea Press, 2018, pp. 339–425.

[23] Loeb, N. G., Wielicki, B. A., Doelling, D. R., Smith, G. L., Keyes, D. F., Kato, S., Manalo-Smith, N., and Wong, T., "Toward Optimal Closure of the Earth's Top-of-Atmosphere Radiation Budget," *Journal of Climate*, Vol. 22, No. 3, Feb. 2009, pp. 748–766.
https://doi.org/10.1175/2008JCLI2637.1

[24] Kato, S., Loeb, N. G., Rutan, D. A., and Rose, F. G., "Clouds and the Earth's Radiant Energy System (CERES) Data Products for Climate Research," *Journal of the Meteorological Society of Japan*, Vol. 93, No. 6, 2015, pp. 597–612.
https://doi.org/10.2151/jmsj.2015-048

[25] Ito, K., and Xiong, K., "Gaussian Filters for Nonlinear Filtering Problems," *IEEE Transactions on Automatic Control*, Vol. 45, No. 5, May 2000, pp. 910–927.
https://doi.org/10.1109/9.855552

[26] Wan, E. A., and Van Der Merwe, R., "The Unscented Kalman Filter for Nonlinear Estimation," *Proceedings of the IEEE 2000 Adaptive Systems for Signal Processing, Communications, and Control Symposium (Cat. No. 00EX373)*, IEEE, New York, 2000, pp. 153–158.
https://doi.org/10.1109/ASSPCC.2000.882463

[27] Julier, S. J., and Uhlmann, J. K., "New Extension of the Kalman Filter to Nonlinear Systems," *Proceedings of the SPIE 3068, Signal Processing, Sensor Fusion, and Target Recognition VI*, Vol. 3068, SPIE, Bellingham, WA, 1997.
https://doi.org/10.1117/12.280797

[28] DaForno, R., Reali, F., Bristor, S., and Debei, S., "Autonomous Navigation of MegSat1: Attitude, Sensor Bias and Scale Factor Estimation by EKF and Magnetometer-Only Measurement," *22nd AIAA International Communications Satellite Systems Conference and Exhibit*, AIAA Paper 2004-3183, May 2004.
https://doi.org/10.2514/6.2004-3183

[29] Sekhavat, P., Gong, Q., and Ross, I. M., "NPSAT 1 Parameter Estimation Using Unscented Kalman Filter," *Proceedings of the 2007 American Control Conference*, IEEE, New York, 2007, pp. 4445–4451.
https://doi.org/10.1109/ACC.2007.4283031

[30] Schaub, H., and Junkins, J. L., *Analytical Mechanics of Space Systems*, 2nd ed., AIAA, Reston, VA, 2009, pp. 122–132.
https://doi.org/10.2514/4.867231

[31] Karlgaard, C. D., and Schaub, H., "Nonsingular Attitude Filtering Using Modified Rodrigues Parameters," *Journal of the Astronautical Sciences*, Vol. 57, No. 4, 2009, pp. 777–791.
https://doi.org/10.1007/BF03321529

[32] Hajiyev, C., and Bahar, M., "Attitude Determination and Control System Design of the ITU-UUBF LEO1 Satellite," *Acta Astronautica*, Vol. 52, Nos. 2–6, 2003, pp. 493–499.
https://doi.org/10.1016/S0094-5765(02)00192-3

[33] Vinther, K., Jensen, K. F., Larsen, J. A., and Wisniewski, R., "Inexpensive CubeSat Attitude Estimation Using Quaternions and Unscented Kalman Filtering," *Automatic Control in Aerospace* Vol. 4, No. 1, 2011, pp. 1–12.

[34] Zanetti, R., Ainscough, T., Christian, J., and Spanos, P. D., "Q Method Extended Kalman Filter [online]," NASA TR JSC-CN-27491, 2012, http://ntrs.nasa.gov/archive/nasa/casi.ntrs.nasa.gov/20120017927.pdf [retrieved 21 Sept. 2020].

[35] Cilden-Guler, D., Raitoharju, M., Piche, R., and Hajiyev, C., "Nanosatellite Attitude Estimation Using Kalman-Type Filters with Non-Gaussian Noise," *Aerospace Science and Technology*, Vol. 92, Sept. 2019, pp. 66–76.
https://doi.org/10.1016/J.AST.2019.05.055

[36] Soken, H. E., Cilden, D., and Hajiyev, C., "Integration of Single-Frame and Filtering Methods for Nanosatellite Attitude Estimation," *Multisensor Attitude Estimation: Fundamental Concepts and Applications*, edited by H. Fourati, and D. E. C. Belkhiat, CRC Press, Boca Raton, FL, 2016, pp. 463–484.
https://doi.org/10.1201/9781315368795

[37] Wahba, G., "Problem 65-1: A Least Squares Estimate of Satellite Attitude," *Society for Industrial and Applied Mathematics Review*, Vol. 7, No. 3, 1965, p. 409.

[38] Cilden-Guler, D., Conguroglu, E. S., and Hajiyev, C., "Single-Frame Attitude Determination Methods for Nanosatellites," *Metrology and Measurement Systems*, Vol. 24, No. 2, 2017, pp. 313–324.

[39] Markley, F. L., and Mortari, D., "Quaternion Attitude Estimation Using Vector Observations," *Journal of the Astronautical Sciences*, Vol. 48, No. 2, 2000, pp. 359–380.

[40] Thébault, E., Finlay, C. C., Beggan, C. D., Alken, P., Aubert, J., Barrois, O., Bertrand, F., Bondar, T., Boness, A., Brocco, L., and Canet, E., "International Geomagnetic Reference Field: The 12th Generation," *Earth, Planets and Space*, Vol. 67, No. 1, 2015, p. 69.
https://doi.org/10.1186/s40623-015-0228-9

[41] Markley, F., and Crassidis, J., "Environment Models," *Fundamentals of Spacecraft Attitude Determination and Control*, Springer, New York, 2014, pp. 403–425.
https://doi.org/10.1007/978-1-4939-0802-8_11

[42] Chen, L., Tang, G., Hu, S., Chen, M., Li, Y., Wang, M., Sun, J., Shi, M., and Li, L., "Earth Polar Motion Parameters High Accuracy Differential Prediction," *Proceedings of the 27th Conference of Spacecraft TT&C Technology in China*, Vol. 323, Lecture Notes in Electrical Engineering, Springer, Heidelberg, 2014, pp. 71–79.
https://doi.org/10.1007/978-3-662-44687-4_7

[43] Snyder, J. P., and Voxland, P. M., *An Album of Map Projections*, Rept. 19.16:1453, U.S. Geological Survey, Washington, D.C., 1989.
https://doi.org/10.3133/pp1453

[44] Khalifa, N. S., and Sharaf-Eldin, T. E., "Earth Albedo Perturbations on Low Earth Orbit Cubesats," *International Journal of Aeronautical and Space Sciences*, Vol. 14, No. 2, 2013, pp. 193–199.
https://doi.org/10.5139/IJASS.2013.14.2.193

[45] Vallado, D. A., and Crawford, P., "SGP4 Orbit Determination," *AIAA/ AAS Astrodynamics Specialist Conference*, AIAA Paper 2008-6770, Aug. 2008.
https://doi.org/10.2514/6.2008-6770

[46] Vallado, D. A., *Fundamentals of Astrodynamics and Applications*, 3rd ed., Vol. 21, Microcosm Press, Hawthorne, CA, 2007.

[47] Burton, R., Rock, S., Springmann, J., and Cutler, J., "Online Attitude Determination of a Passively Magnetically Stabilized Spacecraft," *Acta Astronautica*, Vol. 133, April 2017, pp. 269–281.
https://doi.org/10.1016/j.actaastro.2017.01.024

[48] Hajiyev, C., Cilden, D., and Somov, Y., "Gyro-Free Attitude and Rate Estimation for a Small Satellite Using SVD and EKF," *Aerospace Science and Technology*, Vol. 55, Aug. 2016, pp. 324–331.
https://doi.org/10.1016/j.ast.2016.06.004

O. Abdelkhalik
Associate Editor